Journal of Oceanology and Limnology
Vol. 36 No. 3, P. 651-662, 2018
https://doi.org/10.1007/s00343-018-6352-1

Seasonal variation and modal content of internal tides in the northern South China Sea*

GUO Zheng (郭筝)[1, 2], CAO Anzhou (曹安州)[3], LÜ Xianqing (吕咸青)[1, 2, **]

[1] *Physical Oceanography Laboratory/CIMST, Ocean University of China, Qingdao 266100, China*

[2] *Qingdao National Laboratory for Marine Science and Technology, Qingdao 266100, China*

[3] *Ocean College, Zhejiang University, Zhoushan 316021, China*

Received Jan. 4, 2017; accepted in principle Feb. 14, 2017; accepted for publication Mar. 23, 2017

Abstract A nine-month mooring record was used to investigate seasonal variation and modal content of internal tides (ITs) on the continental slope in the northern South China Sea (SCS). Diurnal tides at this site show clear seasonal change with higher energy in winter than in spring and autumn, whereas semidiurnal tides show the opposite seasonal pattern. The consistency of ITs with barotropic tides within the Luzon Strait, which is the generation region of the ITs, implies that the seasonal variation of ITs depends on their astronomical forcing, even after extended propagation across the SCS basin. Diurnal tides also differ from semidiurnal tides in relation to modal content; they display signals of high modes while semidiurnal tides are dominated by low modes. Reflection of the diurnal tides on the continental slope serves as a reasonable explanation for their high modes. Both diurnal and semidiurnal tides are composed of a larger proportion of coherent components that have a regular 14-day spring-neap cycle. The coherent components are dominated by low modes and they show obvious seasonal variation, while the incoherent components are composed mainly of higher modes and they display intermittent characteristics.

Keyword: internal tide (IT); South China Sea (SCS); seasonal variation; modal content

1 INTRODUCTION

The South China Sea (SCS) has long been identified as a site of intense internal tide (IT) activity due to its characteristic double meridional submarine ridges, strong stratification, and astronomical tides. These strong ITs are considered a primary cause of the enhanced diapycnal mixing and the occurrence of strong nonlinear internal solitary waves in the SCS (Tian et al., 2009; Huang et al., 2016, 2017), which are important for driving or modulating the SCS deep circulation (Zhao et al., 2014; Zhou et al., 2014; Dong et al., 2015). Therefore, ITs in the SCS have been studied in different ways over past decades. For example, Jan et al. (2008) used a three-dimensional tide model to investigate the spatiotemporal variations of baroclinic tides in the Luzon Strait (LS). Vlasenko et al. (2010) focused on the vertical structure of ITs in the SCS in their modeling efforts. In addition to numerical model simulations, in situ data have also been analyzed to further the understanding of the internal wave field of the SCS. Extensive current moorings were deployed around the continental shelf-break area in the northern SCS during the Asian Seas International Acoustic Experiment, enabling the study of ITs and nonlinear internal wave behavior (Duda et al., 2004; Liu et al., 2004; Duda and Rainville, 2008). Using the first comprehensive set of observations obtained during the Internal Waves in Straits Experiment, in combination with high-resolution numerical modeling, Alford et al. (2015) described the complete evolution of internal waves in the SCS. They showed that the waves begin as ITs, steepen

* Supported by the China Postdoctoral Science Foundation (No. 2017M611979), the National Natural Science Foundation of China (Nos. 41606006, 41371496), the Natural Science Foundation of Zhejiang Province (No. LY15D060001), the National High Technology Research and Development Program of China (863 Program) (No. 2013AA09A502), the National Key Technology Research and Development Program (No. 2013BAK05B04), and the 111 Project of Ministry of Education of China (No. B07036)

** Corresponding author: xqinglv@ouc.edu.cn

dramatically as they propagate west from the LS, and then shoal onto the continental slope to the west. Based on satellite altimetric measurements, which provide an important solution to the lack of field observations, Zhao (2014) provided a picture of the propagation and distribution of the K_1, O_1, and M_2 ITs from the LS.

In addition to ITs, the northern SCS has abundant strong mesoscale eddies that arise from the Kuroshio intrusion (Zhang et al., 2013, 2017). Because the Kuroshio intrusion and associated eddy shedding occur primarily in winter (Zhang et al., 2015, 2017), they strongly modulate the seasonal variation of the horizontal and vertical density distribution (or stratification) in the northern SCS. Unsurprisingly, the seasonal density variation in combination with other season-dependent factors (Shaw et al., 2009; Buijsman et al., 2010) results in strong seasonal cycles of ITs (Jan et al., 2008, 2012; Xu et al., 2013; Wu et al., 2013; Liu et al., 2015; Cao et al., 2017). Ma et al. (2013) examined the records of three acoustic Doppler current profilers moored across the continental slope in the northern SCS. They found that diurnal horizontal kinetic energy (HKE) at two of the moorings reached the weakest and strongest seasonal averages in spring and summer, respectively, while there was less seasonal variability of diurnal and semidiurnal tides at the third. Shang et al. (2015) revealed diurnal ITs in the southern SCS are stronger in summer and winter than in spring and autumn; a seasonal variation they attributed to barotropic forcing. Xu et al. (2014) suggested that baroclinic current measurements exhibited north-south asymmetry and temporal variation within the SCS basin. They found the diurnal IT was stronger in summer and winter, while the semidiurnal IT remained invariant. These studies demonstrate the site-dependency of ITs, revealing their different patterns of seasonal variation across the SCS. Therefore, it is worthwhile investigating the seasonality of ITs at different sites to obtain a complete picture of the seasonal behavior of ITs in the SCS and to explore the primary contributing factors. As part of this effort, a record of tidal currents obtained from a mooring located on the edge of the SCS Basin was analyzed. The moored observations were collected as part of the SCS Mesoscale Eddy Experiment (S-MEE), which was designed and conducted in the northern SCS between October 2013 and June 2014 (Zhang et al., 2016, 2017; Huang et al., 2017).

In this paper, we analyze the seasonal variation, modal content, and coherence of both semidiurnal and diurnal ITs in the northern SCS based on one nine-month time series of moored observations. A description of the moored data and the details of their processing are presented in Section 2. In Section 3, we characterize both the vertical structure of the M_2 and K_1 tides, which are the primary tidal constituents within the region, and the coherent and incoherent features of semidiurnal and diurnal signals in different seasons. Factors that contribute to the differences of the semidiurnal and diurnal tides are also discussed. Section 4 provides a summary of this paper.

2 DATA AND METHOD

2.1 Mooring observations

Here, the seasonal variation and modal content of ITs is investigated based on one nine-month time series of near full-depth current velocity data from a mooring located on the continental slope in the SCS (21.11°N, 117.87°E; depth: 950 m) (Fig.1). This mooring was deployed during the S-MEE (the data record starts from 19 August 2013 and ends on 3 June 2014) and it is part of the SCS Mooring Array constructed by the Ocean University of China (Zhang et al., 2016, 2017). The mooring was equipped with an up-looking 75-kHz acoustic Doppler current profiler and a down-looking one at a depth of about 435 m, covering the nominal depth ranges of 45–413 and 413–883 m, respectively. The time interval of the current data used in this study is 1 hour. Details of the instrumental configurations of this mooring can be found in Zhang et al. (2016). For the purposes of analysis, the record is divided into three segments according to season: autumn (September–November), winter (December–February), and spring (March–May).

2.2 Data processing

To identify the principal tidal constituents, power spectral analysis is first performed on data at selected depths. Then, the semidiurnal and diurnal tidal currents at each depth are isolated by bandpass filtering of the raw data using a fourth-order Butterworth filter centered at the frequency bands of 1.73–2.13 and 0.90–1.10 cpd, respectively. Coherent components, which are at deterministic tidal frequencies and phase-locked to the astronomical forcing, are extracted via harmonic analysis. In this study, coherent components are calculated as

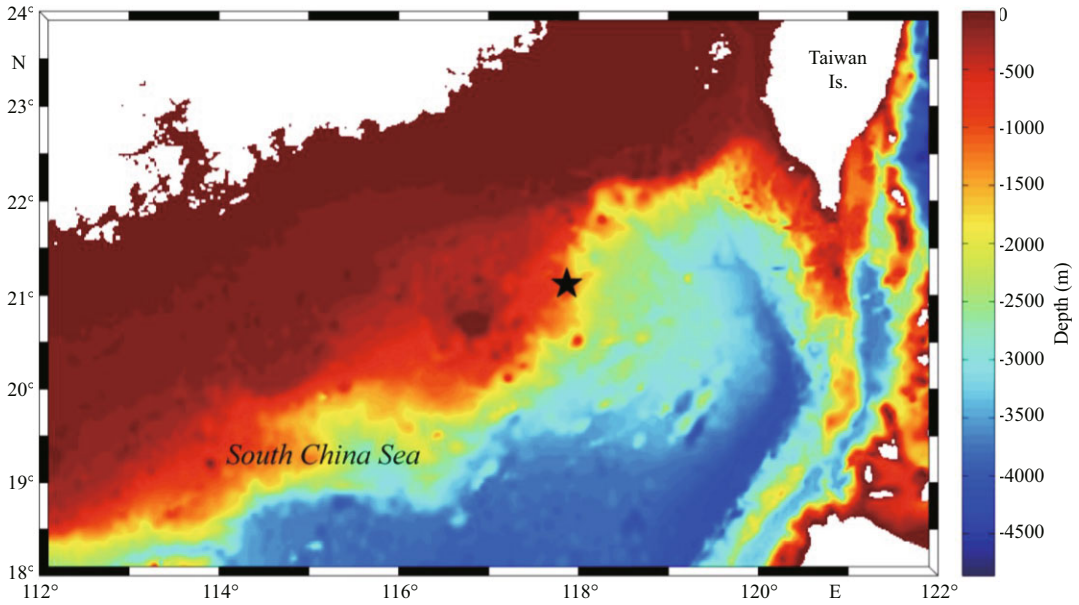

Fig.1 Map of the northern SCS

The mooring is denoted by the black star.

$$u=\sum_{n}H_n\cos(\omega_n t+g_n)\,, \tag{1}$$

where H_n is the amplitude, g_n is the phase, and ω_n is the frequency of the M_2, S_2, N_2, and K_2 for semidiurnal coherent components and the K_1, O_1, P_1, and Q_1 for diurnal coherent components. By subtracting the coherent components from the bandpass filtered current data, the incoherent components are obtained.

The coherent and incoherent semidiurnal signals are next projected onto barotropic and baroclinic modes:

$$\begin{aligned}u(z,t)&=\sum_{m=0}^{\infty}u_m(z,t)\\&=\sum_{m=0}^{\infty}\left[U_m(t)\cdot\partial\varphi_m(z)/\partial z\right]\\&(0<z<h),\end{aligned} \tag{2}$$

where $\partial\varphi_m/\partial z$ is the m-th mode (m=0 represents the barotropic mode and m>0 represents the baroclinic modes) for the horizontal velocity, and U_m is its corresponding coefficient. The modes can be determined by the eigenvalue equation:

$$\begin{cases}\dfrac{\partial^2\phi}{\partial z^2}+\dfrac{N^2}{c^2}\phi=0\\ \phi=0 \quad \text{at} \quad z=0\\ \phi=0 \quad \text{at} \quad z=h\,,\end{cases} \tag{3}$$

where c is the eigenspeed, N is the buoyancy frequency, and h is the water depth. The buoyancy frequency can be calculated using temperature and salinity data from the World Ocean Atlas 2005 (WOA05). Using the Thomson-Haskell method (Thomson, 1950; Haskell, 1953; Fliegel and Hunkins, 1975), the eigenvalue problem can be solved. As can be seen in Fig.2, the climatological stratification profiles merely differ slightly from each other in the upper 200 m. Consequently, the baroclinic modes are computed with the buoyancy frequency averaged over the three seasons. Based on the least square method, U_m can be calculated from the time series of currents and baroclinic modes; thus, the tidal currents of each mode and the full-depth currents can be calculated according to Eq.2. Details of the method of reconstruction of the

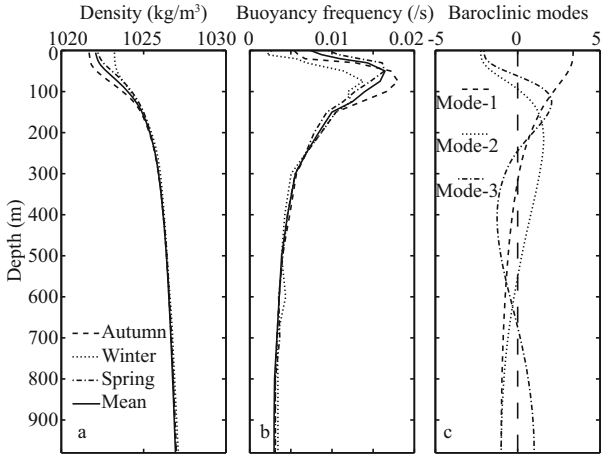

Fig.2 Density (a), buoyancy frequency profiles (b), and vertical structures of baroclinic modes (c) for horizontal velocity in different seasons

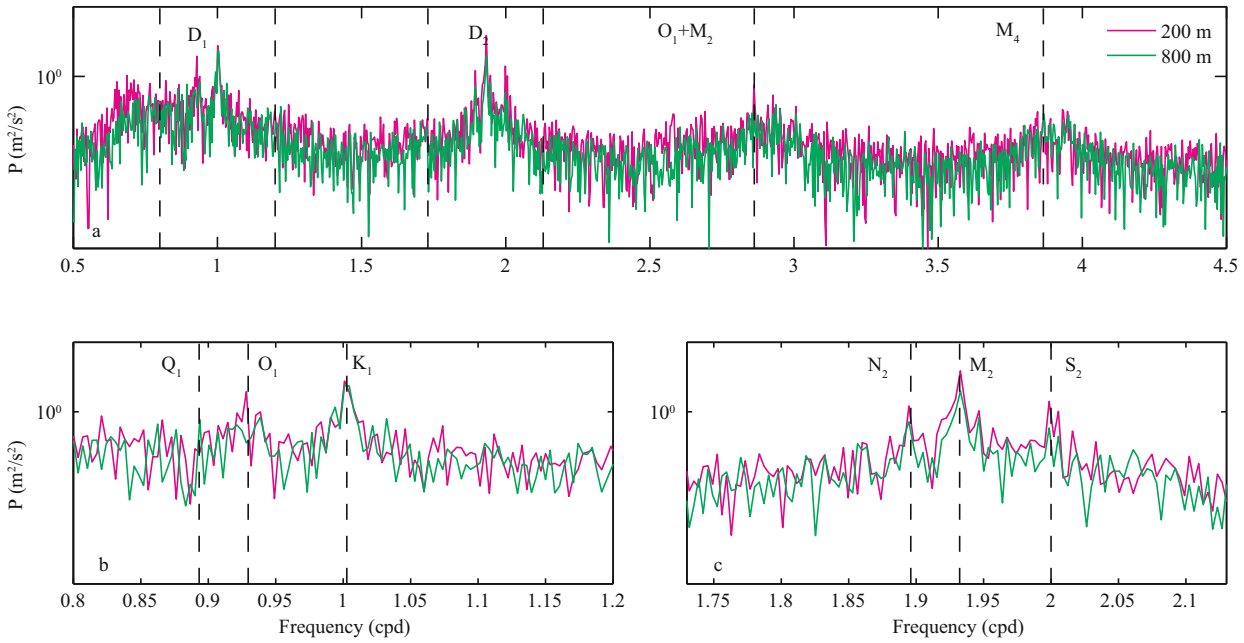

Fig.3 Power spectra of zonal velocity at depths of 200 and 800 m (a); details of the diurnal (b) and semidiurnal (c) constituents are shown in the lower panels

full-depth currents can be found in Cao et al. (2015). Because vertical gaps in the measurements might render the fits of higher modes unstable (Zhao et al., 2012), and because the semidiurnal tides at our site are dominated by lower modes (shown in Section 3), three modes are used for the reconstruction of the semidiurnal tidal currents. Further analysis of the seasonal variations of the semidiurnal ITs is based on these reconstructed currents.

Regarding the diurnal signals, analysis of the modal content is performed in a qualitative manner, because the more complicated vertical structure of the diurnal component (Fig.8) poses a greater challenge for modal decomposition and current reconstruction.

3 RESULT AND DISCUSSION

3.1 Power spectra

Figure 3 shows the power spectra of zonal velocity during the entire study period at depths of 200 and 800 m, representative of the upper and bottom water column, respectively. At both depths, the spectra display the dominance of diurnal and semidiurnal constituents with additional peaks at overtides and compound tides (e.g., O_1+M_2 and M_4) implying a degree of nonlinearity to the IT field. Closer inspection of the semidiurnal frequency band shows that tidal currents are much stronger in the upper layer. The O_1 tidal constituent within the diurnal band also displays a pattern of intensification at the surface, while spectral peaks at the frequencies of K_1 and Q_1 are of similar magnitude, indicating strong currents in both the upper and the bottom layers.

Table 1 Major and minor axes of semidiurnal tidal current ellipses

	Autumn		Winter		Spring	
	Major (cm/s)	Minor (cm/s)	Major (cm/s)	Minor (cm/s)	Major (cm/s)	Minor (cm/s)
M_2	8.6	-3.2	6.0	-1.6	6.2	-2.5
S_2	2.9	-1.3	2.2	-0.7	2.6	-1.3
N_2	2.2	-0.7	2.1	0.3	1.0	-0.03

3.2 Semidiurnal tides

3.2.1 Tidal current ellipses

The power spectra indicate dominance of the M_2 tide in the semidiurnal signal, which is further quantified by harmonic analysis. Tidal ellipse parameters of the principal semidiurnal constituents are calculated using the T-tide toolbox (Pawlowicz et al., 2002). Table 1 displays the major and minor axes of the tidal ellipses of the depth-averaged currents in different seasons. Despite seasonal changes, the M_2 tide is much stronger than the S_2 and N_2 throughout the entire observational period, i.e., the lengths of its axes are at least twice as long as the other tides. Therefore, we investigate further the vertical structure

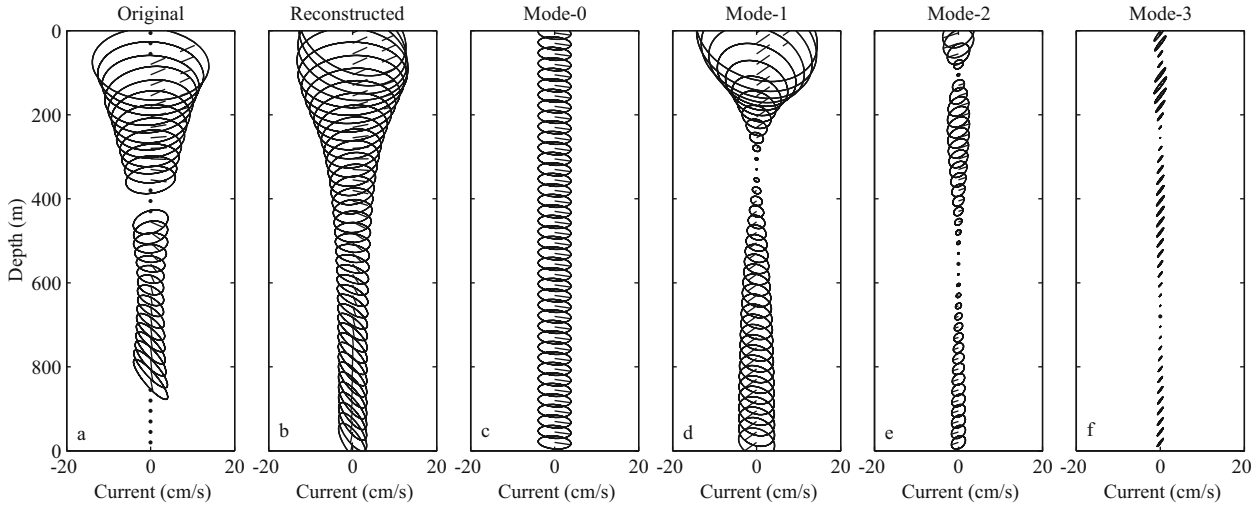

Fig.4 Vertical structures of original (a) and reconstructed (b) M_2 tidal ellipses as well as their corresponding modes (c)–(f)

The ellipses are centered at their corresponding measurement depths and the dashed lines show their local phases at the start time.

of the M_2 elliptical features.

The M_2 tidal currents in each season are first extracted from the full-depth currents reconstructed using the method described in Section 2.2. The results for the winter segment are shown as an example. The absolute errors of the zonal and meridional velocities of the M_2 tide averaged both in depth and in time are 0.33 and 0.26 cm/s, respectively, indicating successful reconstruction. The reconstructed tidal ellipses are consistent with the observed tidal ellipse (Fig.4), showing that currents weaken as depth increases, which confirms the conclusion based on the power spectra. The barotropic mode and the first baroclinic mode dominate the M_2 tidal constituent, while higher modes play less important roles.

Following the same procedure, we can obtain vertical structures of the M_2 tide in different seasons (Fig.5). During the entire observational period, the M_2 tide maintains a similar vertical structure, i.e., both axes of the tidal ellipses reach their maxima in the upper 100 m, decrease rapidly with depth, and remain nearly constant below 400 m. Nevertheless, the M_2 tide does show seasonal variation. It is strongest in autumn and weakest in winter at all depths. To quantify this observation, the depth-integrated HKE averaged over one tidal cycle is computed as

$$\mathrm{HKE}=\frac{1}{2}\int_0^h \rho(z)\left\langle u(z,t)^2+v(z,t)^2\right\rangle \mathrm{d}z, \tag{4}$$

where $u(z, t)$ and $v(z, t)$ are the zonal and meridional velocities, respectively, and the angled brackets indicate the average over one tidal cycle. The calculation results are 3.97, 1.82, and 2.72 kJ/m^2 for autumn, winter, and spring, respectively. It can be found that a 180° transition of the local phase is clearer in autumn and spring, with the node of rapid change fluctuating around the zero-crossing depth of the first baroclinic mode, which implies a larger proportion of the first-mode signal.

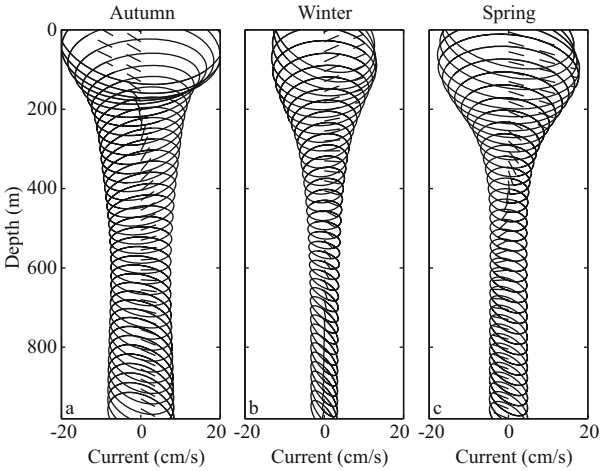

Fig.5 Vertical structures of the reconstructed M_2 tidal ellipses: (a) autumn, (b) winter, and (c) spring

The ellipses are centered at their corresponding measurement depths and the dashed lines show their local phases at the start time.

3.2.2 Coherent and incoherent features

Figure 6 illustrates time-depth graphs of the coherent and incoherent components of the semidiurnal currents. It is evident that the coherent component is apparently much stronger than the incoherent component. In the coherent component, the opposite currents in the shallow and deep waters imply the dominant role of the first baroclinic mode. Conversely, the incoherent component shows multiple

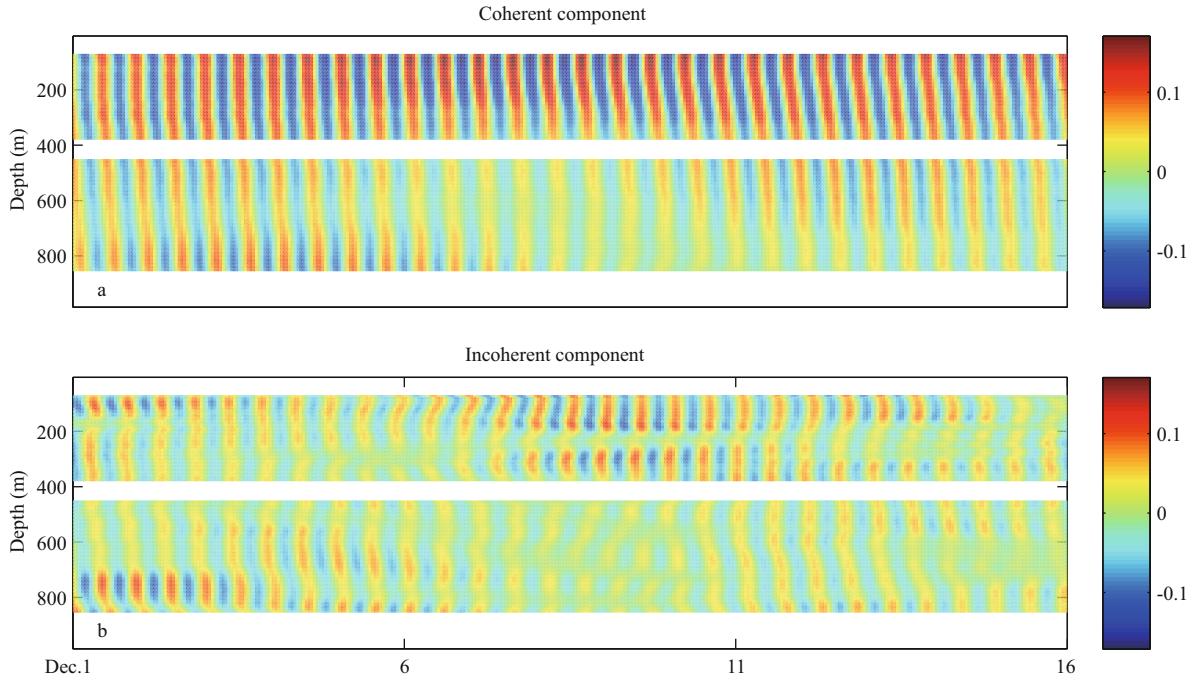

Fig.6 Contours of (a) coherent and (b) incoherent zonal currents of the semidiurnal tides at the mooring site

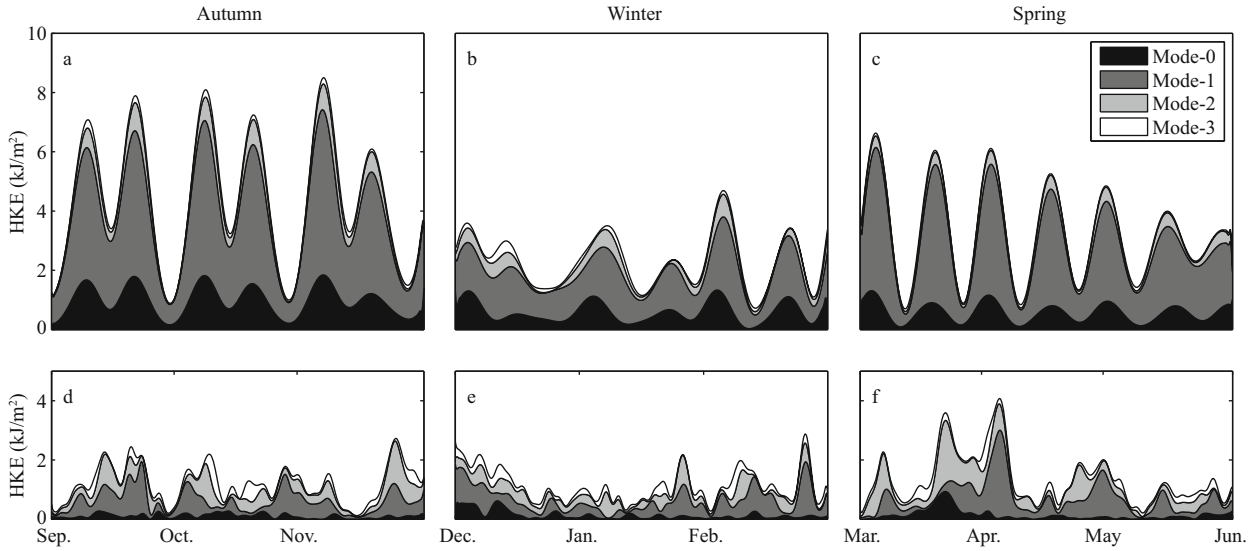

Fig.7 Depth-integrated HKE of semidiurnal (a)–(c) coherent and (d)–(f) incoherent components: (a) and (d) autumn, (b) and (e) winter, and (c) and (f) spring

180° transitions of phase in the vertical direction, which can be attributed to higher modes.

Modal decomposition is performed for the coherent and incoherent components. To measure the contribution of each mode, the depth-integrated HKE is calculated. The HKE of the semidiurnal coherent and incoherent components are plotted as stacked bands colored by mode in Fig.7, and the detailed statistics are presented in Table 2. The modal decomposition results show that the first mode dominates the coherent component with its proportion varying from 57% in winter to 72% in spring. It is followed by mode-0, i.e., the barotropic mode. Higher modes make only minimal contributions. The rises and falls of the barotropic and the baroclinic modes are generally in phase. However, the incoherent component has a different modal structure. The first mode is slightly stronger than the second mode in terms of the seasonal average; however, the first two modes sometimes show comparable magnitudes and

Table 2 Depth-integrated HKE averaged over one tidal period of each mode and its proportion in the semidiurnal coherent or incoherent components (Unit: kJ/m^2)

	Coherent			Incoherent		
	Autumn	Winter	Spring	Autumn	Winter	Spring
Mode-0	0.98 (22%)	0.59 (25%)	0.58 (18%)	0.11 (9%)	0.14 (12%)	0.14 (10%)
Mode-1	2.95 (66%)	1.33 (57%)	2.40 (72%)	0.52 (43%)	0.50 (45%)	0.58 (43%)
Mode-2	0.42 (9%)	0.30 (13%)	0.27 (8%)	0.41 (34%)	0.32 (28%)	0.48 (35%)
Mode-3	0.13 (3%)	0.11 (5%)	0.07 (2%)	0.17 (13%)	0.17 (15%)	0.16 (12%)
Total	4.48	2.33	3.32	1.20	1.13	1.36

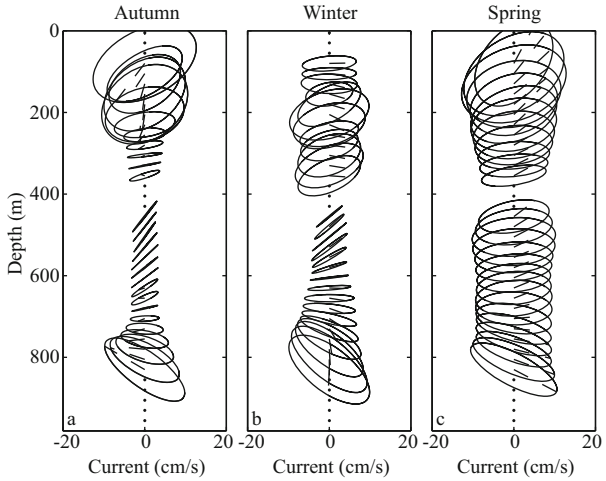

Fig.8 Vertical structures of the K_1 tidal ellipses: (a) autumn, (b) winter, and (c) spring

The ellipses are centered at their corresponding measurement depths and the dashed lines show their local phases at the start time.

they even alternate in assuming the dominant role. Weak as it is, the third mode accounts for a larger proportion of the incoherent component than its counterpart does in the coherent component. The barotropic mode is weakest in the incoherent component. These results confirm the preliminary conclusion drawn from Fig.6, i.e., for semidiurnal ITs at our site, the coherent component is dominated by the first mode while the incoherent component is dominated by higher modes.

Overall, the coherent component is much stronger than the incoherent component; its proportion in the total HKE varies from 79% in autumn to 67% in winter. It has a regular 14-day spring-neap cycle, which is attributed to the modulation of the M_2 and S_2 tides. The coherent component varies with season; its HKE reaches a maximum of 4.48 kJ/m^2 in autumn and a minimum of 2.33 kJ/m^2 in winter. Conversely, the incoherent component shows little seasonal variation, which is consistent with its intermittent nature.

Table 3 Major and minor axes of diurnal tidal current ellipses

	Autumn		Winter		Spring	
	Major (cm/s)	Minor (cm/s)	Major (cm/s)	Minor (cm/s)	Major (cm/s)	Minor (cm/s)
K_1	6.1	-0.9	11.9	-4.1	11.2	-4.9
O_1	3.1	0.5	2.7	0.5	4.7	-0.6
Q_1	0.7	-0.4	0.4	0.2	0.7	-0.1

3.3 Diurnal tides

The continental slope of the northern SCS and the west ridge of the LS are supercritical to diurnal ITs, reflecting and trapping them within the SCS basin (Klymak et al., 2011; Wu et al., 2013). Diurnal tides with a complicated vertical structure contain higher modes, posing considerable challenges to current reconstruction, i.e., producing either unstable solutions for a large number of modes or less accurate solutions for lower modes (Zhao et al., 2012). Therefore, we analyze the characteristics of diurnal tides based on the original data and make a comparison with semidiurnal tides in a qualitative manner.

Harmonic analysis is first conducted on the depth-averaged diurnal signals to identify the most important constituent(s). The major and minor axes of the principal diurnal constituents are shown in Table 3. It is evident that the K_1 tide dominates the others with both its axes being at least two times longer despite the seasonal changes. Consequently, the K_1 is selected for analysis of the vertical structure (Fig.8). Quite different from the M_2, the K_1 tide has a more complicated vertical structure and clearer seasonal variation. In autumn, the K_1 tide intensifies at depths of approximately 80, 200, and 850 m. It shows a similar vertical structure in winter except for weaker currents near the surface. In addition, currents in the middle of the water column are almost rectilinearly polarized in both autumn and winter. In spring, the K_1

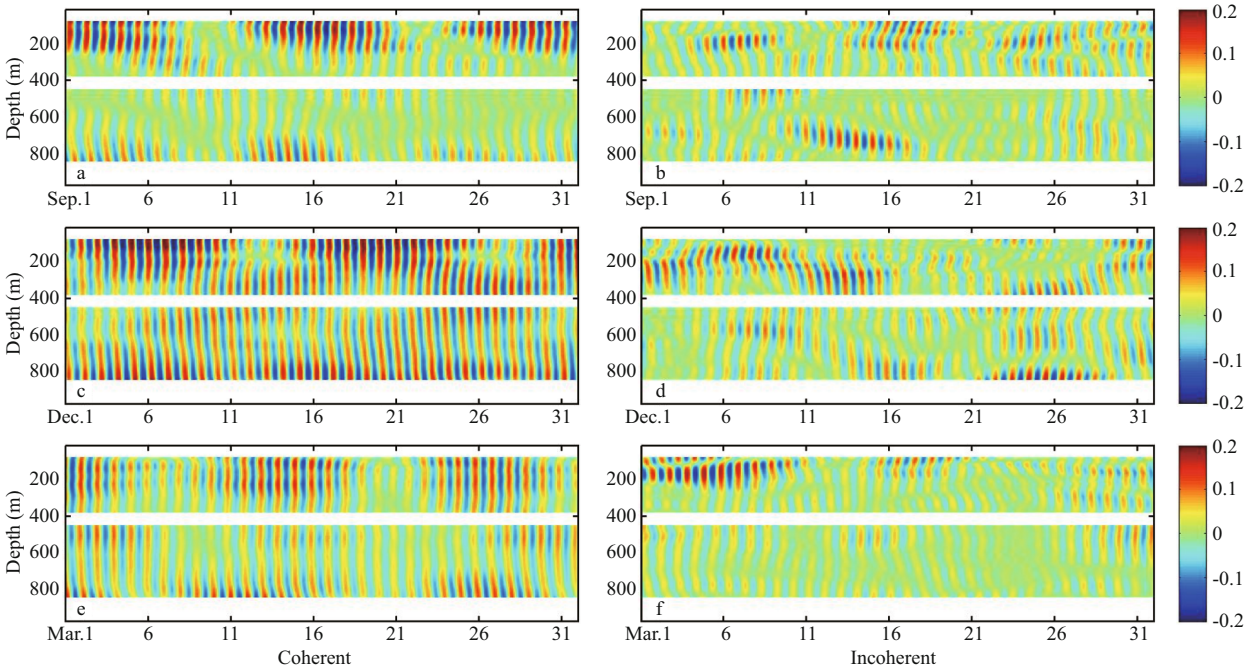

Fig.9 Typical time-depth maps of (a), (c), and (e) coherent and (b), (d), and (f) incoherent diurnal signals

(a) and (b) autumn, (c) and (d) winter, and (e) and (f) spring.

tide becomes much stronger at all depths. The nearly constant amplitudes and phases in the vertical direction imply a dominant role of the barotropic mode.

Coherent and incoherent features are also explored for diurnal signals. Figure 9 shows time-depth maps of zonal currents for a month representative of each season. Similar to those of the semidiurnal tides, the diurnal incoherent components show high wavenumber signals (e.g., the second mode around 16 September and the third mode around 31 December) and intermittent features. The barotropic signal accounts for a large proportion of the coherent component, except for autumn when it is dominated by the first baroclinic mode. A difference in modal content between the coherent and incoherent components has been observed in the southern SCS (Liu et al., 2015). Because of modulation of the K_1 and O_1 tides, the coherent component has a 14-day spring-neap cycle, which is absent from the weaker incoherent constituents. Furthermore, the spring tide in the middle layer is not always in phase with those near the surface and the bottom, possibly due to the reflection of diurnal ITs.

To characterize the seasonal variation of diurnal tides, the depth-integrated HKE is computed as for semidiurnal tides but based on the original diurnal data (Fig.10). Similar to the semidiurnal currents, the coherent component accounts for a larger proportion of the total energy and it shows a regular 14-day spring-neap cycle, consistent with the conclusion drawn from Fig.9. However, its seasonal pattern is different to the semidiurnal coherent component, i.e., stronger in winter than in the other seasons.

3.4 Discussion

Diurnal and semidiurnal ITs on the edge of the SCS basin have different seasonal behaviors, as described above. Semidiurnal tides are weakest in winter when diurnal tides have the greatest energy. Numerical simulations and satellite observations have revealed that ITs in the northern SCS mainly originate from the LS and then propagate westward (Jan et al., 2008; Zhao, 2014). Therefore, it is natural to consider astronomical forcing within the LS for an explanation. Diurnal and semidiurnal barotropic current variances ($\mathrm{Var}=u^2+v^2$) were derived from the Oregon State University Tidal Inversion Software (OTIS, Egbert and Erofeeva, 2002), predictions of which have been proven to agree well with in situ observations around the LS (Ramp et al., 2004; Alford et al., 2011). The variance was also computed for diurnal and semidiurnal coherent components at the mooring and averaged over the entire depth. As shown in Fig.11, the spring-neap cycle of coherent variances is generally in phase with the barotropic forcing in the

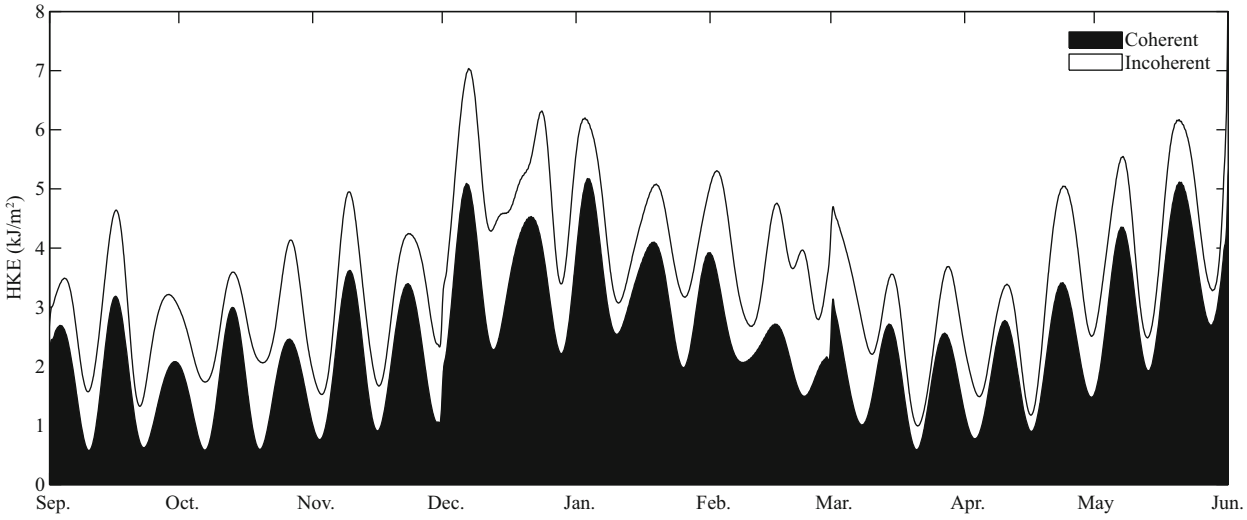

Fig.10 Depth-integrated HKE of diurnal coherent and incoherent components

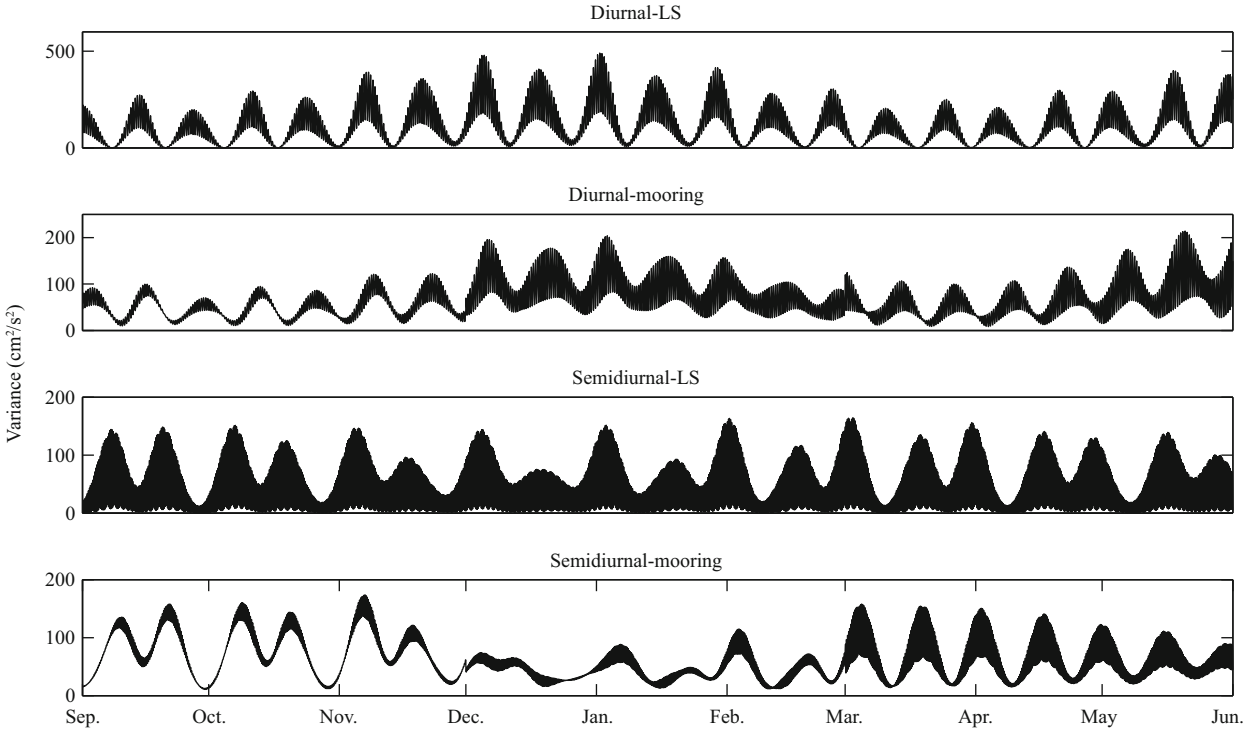

Fig.11 Barotropic current variances in the LS and vertically averaged coherent variances at the mooring for diurnal and semidiurnal frequency bands during the observation period

LS. Furthermore, tidal currents show similar seasonal behaviors at the mooring and at the LS, i.e., the diurnal tides intensify in winter when the semidiurnal tides are weakest. These findings imply that the temporal variation of ITs can be attributed to astronomical forcing at the generation site. Previous studies have revealed that ITs in the deep basin to the west of the LS are mainly modulated by astronomical tides in the LS (Xu et al., 2014). However, ITs on the continental slope and shelf area of the SCS show seasonal patterns different from their astronomical forcing (Guo et al., 2012; Xu et al., 2013). This is explained by the interaction of the ITs with the seasonal thermocline (Xu et al., 2014). Our observations show that ITs on the western edge of the SCS basin maintain the seasonal behavior of their barotropic forcing in the LS. Furthermore, the observations on the continental shelf in those earlier studies were obtained from sites in shallower water to the west of ours. Therefore, we can conclude that it is

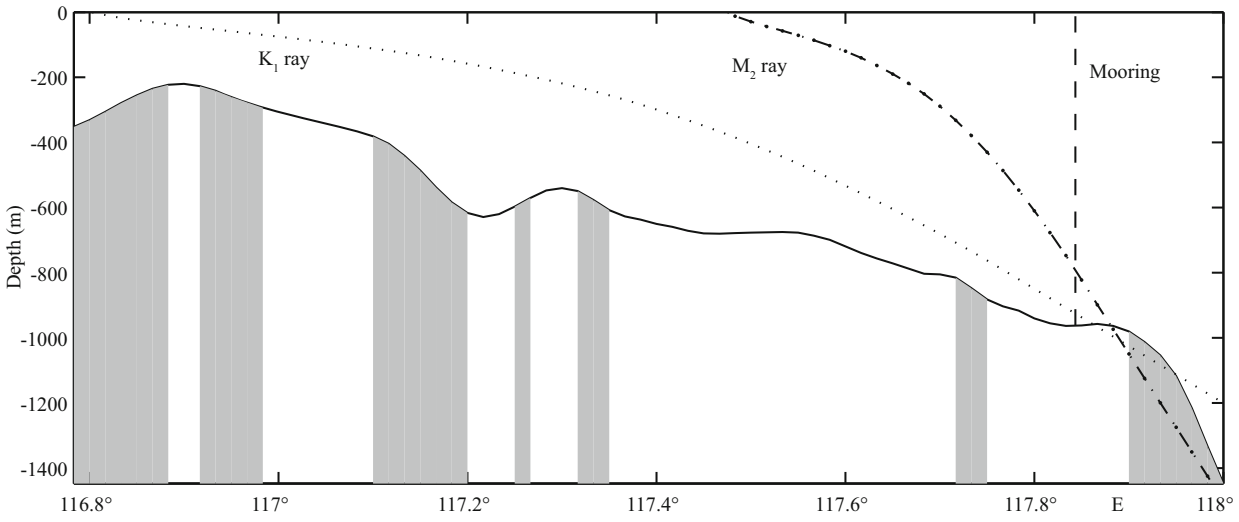

Fig.12 Bathymetry along 21.12°N

Semidiurnal (M_2) and diurnal (K_1) IT characteristics are shown for reference. The region supercritical to the diurnal tide is indicated with gray shading.

in shallower water that the seasonal thermocline has an important effect on the seasonal behavior of ITs.

Diurnal tides also differ from semidiurnal tides in terms of vertical structure, which we attribute to their reflection on the continental slope. Internal waves can transfer their energy to higher wavenumbers after critical reflection (Eriksen, 1982, 1985). Observations have confirmed that the reflection of a mode-1 IT propagating onto the Virginia continental slope can give rise to a higher wavenumber response (Nash et al., 2004). As can be seen in Fig.12, the continental slope to the west to our observation site is supercritical with respect to diurnal tides but subcritical with respect to semidiurnal tides. Reflection of diurnal tides has been observed by Klymak et al. (2011) at two moorings near our site. Therefore, reflection is a reasonable explanation for the higher mode signals at diurnal frequencies (Fig.9b, d, f).

4 SUMMARY

In this study, a nine-month mooring record was analyzed with the objective of characterizing the modal content and seasonal variation of ITs on the edge of the SCS basin. Results show that coherent components of both diurnal and semidiurnal tides have clear seasonal variation and a regular 14-day spring-neap cycle, while incoherent components are more intermittent. They also differ from each other in terms of modal content, i.e., higher modes account for a larger proportion of the incoherent components. Differences exist between the semidiurnal and diurnal signals. The semidiurnal tides are weakest in winter when diurnal tides are strongest. Seasonal patterns of ITs and barotropic tides within the LS, i.e., the generation site of ITs, show good agreement. This implies that the seasonal behavior of ITs is dictated by their astronomical forcing, even after extended propagation across the SCS basin, rather than by interaction with the thermocline. In terms of the vertical structure, the diurnal signals contain a greater number of higher modes, which is different from the domination of low modes in semidiurnal ITs. A reasonable explanation for this is reflection of the diurnal tide from the supercritical slope.

5 ACKNOWLEDGEMENT

The mooring data used this paper were obtained by the South China Sea Mooring Array constructed by the Ocean University of China. The authors deeply thank Professor TIAN Jiwei for providing the mooring data.

References

Alford M H, MacKinnon J A, Nash J D, Simmons H, Pickering A, Klymak J M, Pinkel R, Sun O, Rainville L, Musgrave R, Beitzel T, Fu K H, Lu C W. 2011. Energy flux and dissipation in Luzon Strait: two tales of two ridges. *Journal of Physical Oceanography*, **41**(11): 2 211-2 222.

Alford M H, Peacock T, MacKinnon J A et al. 2015. The formation and fate of internal waves in the South China Sea. *Nature*, **521**(7550): 65-69.

Buijsman M C, Kanarska Y, McWilliams J C. 2010. On the generation and evolution of nonlinear internal waves in the South China Sea. *Journal of Geophysical Research*, **115**(C2): C02012.

Cao A Z, Guo Z, Lv X Q, Song J B, Zhang J C. 2017. Coherent and incoherent features, seasonal behaviors and spatial variations of internal tides in the northern South China Sea. *Journal of Marine Systems*, **172**: 75-83.

Cao A Z, Li B T, Lv X Q. 2015. Extraction of internal tidal currents and reconstruction of full-depth tidal currents from mooring observations. *Journal of Atmospheric and Oceanic Technology*, **32**(7): 1 414-1 424.

Dong J H, Zhao W, Chen H T, Meng Z C, Shi X C, Tian J W. 2015. Asymmetry of internal waves and its effects on the ecological environment observed in the northern South China Sea. *Deep Sea Research Part I*: *Oceanographic Research Papers*, **98**: 94-101.

Duda T F, Lynch J F, Irish J D, Beardsley R C, Ramp S R, Chiu C S, Tang T Y, Yang Y J. 2004. Internal tide and nonlinear internal wave behavior at the continental slope in the northern South China Sea. *IEEE Journal of Oceanic Engineering*, **29**(4): 1 105-1 130.

Duda T F, Rainville L. 2008. Diurnal and semidiurnal internal tide energy flux at a continental slope in the South China Sea. *Journal of Geophysical Research*, **113**(C3): C03025.

Egbert G D, Erofeeva S Y. 2002. Efficient inverse modeling of Barotropic ocean tides. *Journal of Atmospheric and Oceanic Technology*, **19**(2): 183-204.

Eriksen C C. 1982. Observations of internal wave reflection off sloping bottoms. *Journal of Geophysical Research*, **87**(C1): 525-538.

Eriksen C C. 1985. Implications of ocean bottom reflection for internal wave spectra and mixing. *Journal of Physical Oceanography*, **15**(9): 1 145-1 156.

Fliegel M, Hunkins K. 1975. Internal wave dispersion calculated using the Thomson-Haskell method. *Journal of Physical Oceanography*, **5**(3): 541-548.

Guo P, Fang W D, Liu C J, Qiu F W. 2012. Seasonal characteristics of internal tides on the continental shelf in the northern South China Sea. *Journal of Geophysical Research*, **117**(C4): C04023.

Haskell N A. 1953. The dispersion of surface waves on multilayered media. *Bulletin of the Seismological Society of America*, **43**(1): 17-34.

Huang X D, Chen Z H, Zhao W, Zhang Z W, Zhou C, Yang Q X, Tian J W. 2016. An extreme internal solitary wave event observed in the northern South China Sea. *Scientific Reports*, **6**: 30041, https://doi.org/10.1038/srep30041.

Huang X D, Zhang Z W, Zhang X J, Qian H B, Zhao W, Tian J W. 2017. Impacts of a mesoscale eddy pair on internal solitary waves in the northern South China Sea revealed by mooring array observations. *Journal of Physical Oceanography*, https://doi.org/10.1175/JPO-D-16-0111.1.

Jan S, Chern C S, Wang J, Chiou M D. 2012. Generation and propagation of baroclinic tides modified by the Kuroshio in the Luzon Strait. *Journal of Geophysical Research*, **117**(C2): C02019.

Jan S, Lien R C, Ting C H. 2008. Numerical study of baroclinic tides in Luzon Strait. *Journal of Oceanography*, **64**(5): 789-802.

Klymak J M, Alford M H, Pinkel R, Lien R C, Yang Y J, Tang T Y. 2011. The breaking and scattering of the internal tide on a continental slope. *Journal of Physical Oceanography*, **41**(5): 926-945.

Liu A K, Ramp S R, Zhao Y H, Tang T Y. 2004. A case study of internal solitary wave propagation during ASIAEX 2001. *IEEE Journal of Oceanic Engineering*, **29**(4): 1 144-1 156.

Liu J L, He Y H, Wang D X, Liu T Y, Cai S Q. 2015. Observed enhanced internal tides in winter near the Luzon Strait. *Journal of Geophysical Research*, **120**(10): 6 637-6 652.

Liu Q, Xie X H, Shang X D, Chen G Y. 2016. Coherent and incoherent internal tides in the southern South China Sea. *Chinese Journal of Oceanology and Limnology*, **34**(6): 1 374-1 382.

Ma B B, Lien R C, Ko D S. 2013. The variability of internal tides in the Northern South China Sea. *Journal of Oceanography*, **69**(5): 619-630.

Nash J D, Kunze E, Toole J M, Schmitt R W. 2004. Internal tide reflection and turbulent mixing on the continental slope. *Journal of Physical Oceanography*, **34**(5): 1 117-1 134.

Pawlowicz R, Beardsley B, Lentz S. 2002. Classical tidal harmonic analysis including error estimates in MATLAB using T_TIDE. *Computers & Geosciences*, **28**(8): 929-937.

Ramp S R, Tang T Y, Duda T F, Lynch J F, Liu A K, Chiu C S, Bahr F L, Kim H R, Yang Y J. 2004. Internal solitons in the northeastern South China Sea. Part I: sources and deep water propagation. *IEEE Journal of Oceanic Engineering*, **29**(4): 1 157-1 181.

Shang X D, Liu Q, Xie X H, Chen G Y, Chen R Y. 2015. Characteristics and seasonal variability of internal tides in the southern South China Sea. *Deep Sea Research Part I*: *Oceanographic Research Papers*, **98**: 43-52.

Shaw P T, Ko D S, Chao S Y. 2009. Internal solitary waves induced by flow over a ridge: with applications to the northern South China Sea. *Journal of Geophysical Research*, **114**(C2): C02019.

Thomson W T. 1950. Transmission of elastic waves through a stratified solid medium. *Journal of Applied Physics*, **21**(2): 89-93.

Tian J W, Yang Q X, Zhao W. 2009. Enhanced diapycnal mixing in the South China Sea. *Journal of Physical Oceanography*, **39**(12): 3 191-3 203, https://doi.org/10.1175/2009JPO3899.1.

Vlasenko V, Stashchuk N, Guo C, Chen X. 2010. Multimodal structure of baroclinic tides in the South China Sea. *Nonlinear Processes in Geophysics*, **17**(5): 529-543.

Wu L D, Miao C B, Zhao W. 2013. Patterns of K_1 and M_2 internal tides and their seasonal variations in the northern South China Sea. *Journal of Oceanography*, **69**(4): 481-494.

Xu Z H, Yin B S, Hou Y J, Liu A K. 2014. Seasonal variability and north-south asymmetry of internal tides in the deep basin west of the Luzon Strait. *Journal of Marine Systems*, **134**: 101-112.

Xu Z H, Yin B S, Hou Y J, Xu Y S. 2013. Variability of internal

tides and near-inertial waves on the continental slope of the northwestern South China Sea. *Journal of Geophysical Research*, **118**(1): 197-211.

Zhang Z W, Tian J W, Qiu B, Zhao W, Chang P, Wu D X, Wan X Q. 2016. Observed 3D structure, generation, and dissipation of oceanic mesoscale eddies in the South China Sea. *Scientific Reports*, **6**: 24 349.

Zhang Z W, Zhao W, Qiu B, Tian J W. 2017. Anticyclonic eddy sheddings from Kuroshio loop and the accompanying cyclonic eddy in the northeastern South China Sea. *Journal of Physical Oceanography*, https://doi.org/10.1175/JPO-D-16-0185.1.

Zhang Z W, Zhao W, Tian J W, Liang X F. 2013. A mesoscale eddy pair southwest of Taiwan and its influence on deep circulation. *Journal of Geophysical Research*, **118**(12): 6 479-6 494.

Zhang Z W, Zhao W, Tian J W, Yang Q X, Qu T D. 2015. Spatial structure and temporal variability of the zonal flow in the Luzon Strait. *Journal of Geophysical Research*, **120**(2): 759-776.

Zhao W, Zhou C, Tian J W, Yang Q X, Wang B, Xie L L, Qu T D. 2014. Deep water circulation in the Luzon Strait. *Journal of Geophysical Research*, **119**(2): 790-804.

Zhao Z X, Alford M H, Lien R C, Gregg M C, Carter G S. 2012. Internal tides and mixing in a submarine canyon with time-varying stratification. *Journal of Physical Oceanography*, **42**(12): 2 121-2 142.

Zhao Z X. 2014. Internal tide radiation from the Luzon Strait. *Journal of Geophysical Research*, **119**(8): 5 434-5 448.

Zhou C, Zhao W, Tian J W, Yang Q X, Qu T D. 2014. Variability of the deep-water overflow in the Luzon strait. *Journal of Physical Oceanography*, **44**(11): 2 972-2 986.